Nano Energy 56 (2019) 840–850

Contents lists available at ScienceDirect

Nano Energy

journal homepage: www.elsevier.com/locate/nanoen

Full paper

Ferroelectric polarization promoted bulk charge separation for highly efficient CO_2 photoreduction of $SrBi_4Ti_4O_{15}$

Shuchen Tu[a], Yihe Zhang[a,*], Ali H. Reshak[b], Sushil Auluck[c], Liqun Ye[d], Xiaopeng Han[e], Tianyi Ma[f,*], Hongwei Huang[a,*]

[a] Beijing Key Laboratory of Materials Utilization of Nonmetallic Minerals and Solid Wastes, School of Materials Science and Technology, China University of Geosciences, Beijing 100083, China
[b] Nanotechnology and Catalysis Research Center (NANOCAT), University of Malaya, 50603 Kuala Lumpur, Malaysia
[c] CSIR- National Physical Laboratory, Dr. K S, Krishnan Road, New Delhi, 110012, India.
[d] Key Laboratory of Ecological Security for Water Source Region of Mid-line Project of South-to-North Water Diversion of Henan Province, College of Chemistry and Pharmaceutical Engineering, Nanyang Normal University, Nanyang 473061, China
[e] School of Materials Science and Engineering, Tianjin Key Laboratory of Composite and Functional Materials, Tianjin University, Tianjin 300072, China
[f] School of Environmental and Life Sciences, The University of Newcastle (UON), Callaghan, NSW 2308, Australia

ARTICLE INFO

Keywords:
Spontaneous polarization
Ferroelectric perovskite
Piezoelectric-catalysis
$SrBi_4Ti_4O_{15}$ nanosheets
CO_2 photoreduction

ABSTRACT

Fast recombination of photogenerated charge carriers in bulk remains the major obstacle for photocatalysis nowadays. Developing ferroelectrics directly as photoactive semiconducting catalysts may be promising in view of the strong ferroelectric polarization that induces the anisotropic charge separation. Here, we report a ferroelectric layered perovskite $SrBi_4Ti_4O_{15}$ as a robust photocatalyst for efficient CO_2 reduction. In the absence of co-catalysts and sacrificial agents, the annealed $SrBi_4Ti_4O_{15}$ nanosheets with the strongest ferroelectricity cast a prominent photocatalytic CO_2 reduction activity for CH_4 evolution with a rate of 19.8 μmol h^{-1} g^{-1} in the gas-solid reaction system, achieving an apparent quantum yield (AQY) of 1.33% at 365 nm, outperforming most of the reported photocatalysts. The ferroelectric hysteresis loop, piezoresponse force microscopy (PFM) and ns-level time-resolved fluorescence spectra uncover that the outstanding CO_2 photoreduction activity of $SrBi_4Ti_4O_{15}$ mainly stems from the strong ferroelectric spontaneous polarization along [100] direction, which allows efficient bulk charge separation along opposite direction. DFT calculations also disclose that both electrons and holes show the smallest effective masses along *a* axis, verifying the high mobility of charge carriers facilitated by ferroelectric polarization. This study suggests that the traditionally semiconducting ferroelectric materials that have long been studied as ferro/piezoelectric ceramics now may be powerfully applied in the photocatalytic field to deal with the growing energy crisis.

1. Introduction

Solar-light driven CO_2 conversion into renewable fuels shows tremendous potentials in recent years [1–4], whereas it remains highly challenging owing to the inertness of CO_2 molecules at ambient atmosphere and the low efficiency of photocatalysts as the recombination rate of photoinduced charge carriers is several orders quicker than the separation rate [5]. Attempts aimed to suppress the recombination of photogenerated electrons and holes by establishing an effective electric field harvest considerable attentions [6–9]. Particularly, it is demonstrated lately that introduction of a polarized electric field via coupling a ferroelectric could drastically facilitates the separation and migration of charge carriers of a photocatalyst.

For instance, the spontaneous polarization generated from ferroelectric $SrTiO_3$ largely improves the charge separation efficiency of TiO_2 photoelectrode, thus giving rising to a high photoelectrochemical (PEC) water splitting performance [9]. Ferroelectric $BiFeO_3$ was also demonstrated capable of decreasing the charge recombination rate of $BiVO_4$ photoanode from 17 s^{-1} to 0.6 s^{-1}, which allows an increased PEC oxygen evolution rate by ~4.4 times [10]. The enhancement was mainly attributed to the strong spontaneous polarization derived from the displacement of the positive and negative charge centers in ferroelectrics that rendered generation of macroscopic polarization charges on the opposite sides, which induced the high separation of photo-excited charge carriers on the surface of photocatalysts [11]. However, these ferroelectric materials only served as co-catalysts to strengthen

* Corresponding authors.
E-mail addresses: zyh@cugb.edu.cn (Y. Zhang), Tianyi.Ma@newcastle.edu.au (T. Ma), hhw@cugb.edu.cn (H. Huang).

https://doi.org/10.1016/j.nanoen.2018.12.016
Received 30 October 2018; Received in revised form 26 November 2018; Accepted 7 December 2018
Available online 08 December 2018
2211-2855/

the surface/interfacial charge migration, while high bulk charge recombination of photo(electro)catalysis still existed [12]. In view of the strong macroscopic polarization across the bulk material in ferroelectrics, developing them as semiconducting photocatalysts should be appealing. Nevertheless, seldom ferroelectrics were reported directly as photoactive catalysts so far, particularly for the photocatalytic reduction of inert CO_2.

Layered bismuth-based semiconductor materials recently gain great efforts from researchers for the unique structural characteristics, namely, layered configuration consisting of $(Bi_2O_2)^{2+}$ slices and interleaved negatively-charged ions/polyhedra layers [13], which forms an electrostatic field for promoting the separation of charge carriers [14]. $SrBi_4Ti_4O_{15}$ is located at the intersection of traditional ferroelectric, layered bismuth-based semiconductor and perovskite-structured crystal, which may gather all the above benefits and show great potential for photocatalysis. Nonetheless, the current studies on $SrBi_4Ti_4O_{15}$ all focus on its applications for ferroelectric ceramics, and not any photocatalytic properties have been reported. Additionally, almost all the reported $SrBi_4Ti_4O_{15}$ ferroelectric ceramics are synthesized through high-temperature solid-state reaction, which leads to insufficient reactive sites, unfavorable for high photocatalytic acivity. Therefore, development of nanostructured $SrBi_4Ti_4O_{15}$ with large ferroelectricity for high-efficiency photocatalytic CO_2 are highly desirable, and it is of great significance to disclose the relationship between photocatalysis and ferroelectricity.

Herein, we report the synthesis of $SrBi_4Ti_4O_{15}$ nanosheets by a soft-chemical route via introduction of sodium hydrate as a mineralizer. To elucidate the structural-property relationship, annealing post-treatment is adopted as a productive strategy to tune ferroelectric polarization of $SrBi_4Ti_4O_{15}$. It is demonstrated that the $SrBi_4Ti_4O_{15}$ nanosheets annealed at 350 °C show the largest ferroelectricity, which also display the most efficient charge seperation efficiency. This advanced material thus casts a prominent photocatalytic CO_2 reduction activity for CH_4 evolution with a rate of 19.8 μmol h^{-1} g^{-1} without any co-catalysts or sacrificial agents in the gas-solid reaction system, and a high apparent quantum efficiency of 1.33% at 365 nm was achieved, outperforming most of semiconductor photocatalysts.

2. Experimental details

2.1. Sample preparation

All chemicals used in this work were analytical reagent grade without further purification process. $SrBi_4Ti_4O_{15}$ was synthesized by a hydrothermal method. In a typical operation, 1.12 g tetra-butyl titanate (Beijing Chemical Industry Group Co., Ltd) was added and dispersed into a 30 mL of NaOH (Beijing Chemical Industry Group Co., Ltd) solution (3 M) at room temperature. Then, a certain amount of bismuth nitrate pentahydrate (Xilong Scientific Co., Ltd.) and strontium chloride (Xilong Scientific Co., Ltd.) was added to the above solution with the Bi: Sr: Ti molar ratio of 4: 1: 4, and the mixed solution was continuously magnetic-stirred for 0.5 h and ultrasonic-dispersed before being transferred into a 50 mL Teflon-lined stainless autoclave and heated at 180 °C for 20 h. After cooling, the products were filtered, and washed with deionized water and absolute ethyl alcohol for each 3 times, the obtained samples were collected and dried at 80 °C in air for 6 h. P25 was purchased from the Jingwen chemical reagent company, and BiOBr was obtained by a simple hydrolysis method [15], and the $Bi_4Ti_3O_{12}$ was prepared by an hydrothermal method [16]. It is reported that annealing treatment can largely affect the ferroelectricity [17,18]. For obtaining samples with altering spontaneous polarization and further studying the relationship between ferroelectric polarization and photocatalysis, the as-prepared $SrBi_4Ti_4O_{15}$ nanosheets (SBTO-1) were annealed at 350 °C (SBTO) and 650 °C (SBTO-2) in a resistance furnace for 2 h to tune the ferroelectricity of $SrBi_4Ti_4O_{15}$, respectively.

2.2. Characterization

X-ray diffraction (XRD) was conducted on a Bruker D8 diffractometer with Cu Kα radiation to analyze the crystalline structure of obtained samples. The X-ray photoelectron spectroscopy (XPS, ESCALAB 250 Xi ThermoFisher, UK) was used to analyze the chemical compositions of the as-synthesized samples. The morphology and microstructure of the products were investigated by S-4800 scanning electron microscope (SEM), and energy dispersive spectroscopy (EDS) attached to the SEM was used to examine the composition of the products at the same time. Transmission electron microscopy (TEM) and high-resolution transmission electron microscopy (HRTEM) images were obtained using a JEM-2100 electron microscopy (JEOL, Japan). Specific surface areas of the samples were characterized by the nitrogen adsorption BET method with a Micromeritics 3020 instrument. UV–vis diffuse reflectance spectra (DRS) were recorded from a PerkinElmer Lambda 35 UV–vis spectrometer. The spectra were collected at 200–800 nm, referenced to BaSO4. Photoluminescence (PL) spectra of the as-prepared samples were measured using a Hitachi F-4600 fluorescence spectrophotometer (Tokyo, Japan) to determine the recombination rate of electron–hole pairs. The fluorescence lifetime was determined by time-resolved fluorescence emission spectra on a fluorescence spectrophotometer (Edinburgh Instruments, FLSP-920), and the applied excitation wavelength was 404 nm.

2.3. Mott-schottky curve measurements

For determining the flat band potential, Mott-Schottky curves were measured on an electrochemical analyzer (CHI 660E, Shanghai) equipped with a systematic three-electrode pattern, in which the samples coated on ITO glass serve as the working electrode. Pt wire is used as the counter electrode and saturated calomel electrode is applied as the reference electrode. In the dip-coating process, 50 mg of photocatalyst was dispersed into 5 mL of ethanol to obtain uniform suspending liquid before being dropwise added on an indium–tin oxide (ITO) glass. Then the working electrode was dried at 373 K for 10 h to remove ethanol. Xe lamp (300 W) was used as the irradiation source and the measurement was carried out in a 0.1 M Na_2SO_4 solution.

2.4. Photocatalytic CO_2 reduction test

The photocatalytic CO_2 reduction experiments were conducted in a gas-solid reaction system with a Lab solar-III AG closed circulation system (Beijing Perfect light Technology Co., Ltd., China). 0.1 g of photocatalyst was ultrasonically dispersed in deionized water and poured into the sample stage. Then, the dispersion was dried at 80 ℃ for 12 h to create a thin film in sample stage upper standing in the vacuum reactor. Thereafter, 1.3 g of $NaHCO_3$ was uniformly placed at the bottom of the vacuum reactor. Subsequently, 15 mL of H_2SO_4 (1.33 M) was injected into the bottom of vacuum reactor to react with $NaHCO_3$ to in situ generate CO_2 (1 atm). Xe lamp (300 W) was used as light source to irradiate the reactor with photoreaction temperature keeping at 20 ℃. After that, 1 mL of gas was taken for subsequent qualitative analysis by GC9790II gas chromatography (Zhejiang Fuli Analytical Instrument Co.), and the produced CO, CH_4 and O_2 were all detected at the same time. 365 nm monochromatic light (365 nm band-pass filter) is used to test the apparent quantum efficiency (AQE) by the following equation [19]:

$$AQY(\%) = (number\ of\ reacted\ electrons / number\ of\ incident\ photons) \times 100\%$$
$$= [(2 \times number\ of\ evolved\ CO\ molecules + 8 \times number\ of\ evolved\ CH_4\ molecules) / number\ of\ incident\ photons] \times 100\%.$$

2.5. Ferroelectric and piezoresponse force microscopy (PFM) measurements

The ferroelectric properties of $SrBi_4Ti_4O_{15}$ samples were measured by a ferroelectric tester (AixACCT, TF Analyzer 2000, Germany). The $SrBi_4Ti_4O_{15}$ sample was pressed in a pellet (~10 mm diameter and ~0.8 mm thick). Then the pellets were annealed at 350 °C and 650 °C, and the silver paste was applied to both sides of the pellet [20]. A voltage of 900 V at 1 Hz was applied. Piezoresponse force microscopy (PFM) measurements of the $SrBi_4Ti_4O_{15}$ were performed with Oxford MFP-3D AFM (Oxford MFP-3D, UK). The $SrBi_4Ti_4O_{15}$ samples were dispersed in ethyl alcohol, and then were distributed on the silicon substrate by a spin coating method.

2.6. Density functional theory (DFT) calculation

DFT calculation is carried out by utilizing CASETP code implemented plane wave method and Perdew-Burke-Ernzerhof function for getting density of states and electronic band structure of $SrBi_4Ti_4O_{15}$. A discrete k mesh along the high-symmetry directions of band structures was calculated by VASP to obtain the effective mass along the different directions. The carrier effective mass is evaluated from the second derivative of the highest point of the VB band and the lowest point of the CB band according to $E = \hbar^2k^2/2\,m_em^*$, where m_e denotes the free electron mass (9.1×10^{-19} kg) [21].

3. Results and discussion

3.1. Characterization of layered $SrBi_4Ti_4O_{15}$ nanosheets

$SrBi_4Ti_4O_{15}$ crystallizes in the polar non-centrosymmetric (NCS) space group $A2_1am$. It presents a typical Aurivillius-type layered crystal structure consisting of $(Bi_2O_2)^{2+}$ slices and alternatively interleaved four-layers TiO_6 octahedra along the *c* axis (Fig. 1a), and Sr and Bi atoms co-occupy the A site in the caves of four-layers TiO_6 octahedra. The displacement of positive and negtive charge centers in TiO_6 octahedra (Table S1) produces spontaneous polarization. $SrBi_4Ti_4O_{15}$ nanosheets were synthesized for the first time via a one-pot hydrothermal process with $Bi(NO_3)_3{\cdot}5H_2O$, tetrabutyl titanate and $SrCl_2{\cdot}2H_2O$ as the reactants, and NaOH (3 M) was employed as a mineralizer. Here, the introduction of NaOH is critical for synthesis of $SrBi_4Ti_4O_{15}$ nanosheets. The strong basicity of concentrated NaOH solution allows TiO_2 to hydrolyze from tetrabutyl titanate into dissolved titanate; the homogeneous reaction solution is beneficial for formation of nanostructure. Without addition of NaOH, no $SrBi_4Ti_4O_{15}$ products were yielded, and too low or too high NaOH concentration was also unfavorable for obtaining the pure-phase product. The X-ray diffraction (XRD) pattern is well indexed to the orthorhombic phase $SrBi_4Ti_4O_{15}$ (PDF #43–0973), confirming the successful preparation of pure $SrBi_4Ti_4O_{15}$ (Fig. 1b). The broadened diffraction peaks indicate the presence of nanostructure. The obviously high intensity of (020) peak with the reference diffractogram suggests the preferential exposing of (001) facet [22], which is also confirmed by the following transmission electron microscopy (TEM) images.

The as-obtained $SrBi_4Ti_4O_{15}$ present a nanosheet structure (plate size of 0.2–0.5 μm, see Fig. S1 for a SEM image), and TEM confirms the well dispersed nanoflakes (Fig. 1c). The interplanar spacing of lattice fringe of $SrBi_4Ti_4O_{15}$ was measured to be ~0.278 and 0.271 nm, corresponding to (200) and (020) planes, respectively. Therefore, the exposed facet of $SrBi_4Ti_4O_{15}$ is the {001} facet (Fig. 1c and d). The selected area electron diffraction (SAED) pattern is also assigned to the [001] zone-axis diffraction spots. TEM-EDX elemental maps (Fig. 1d) reveal the homogeneous distribution of Sr, Bi, Ti and O across $SrBi_4Ti_4O_{15}$ nanosheets. UV–vis diffuse reflectance spectra (DRS) demonstrate that $SrBi_4Ti_4O_{15}$ nanosheets exhibit an absorption edge at around 420 nm (Fig. 1f), which accords with the pale yellow color (Fig. S2). The photoabsorption of $SrBi_4Ti_4O_{15}$ is similar to that of the typical bismuth-based semiconductors BiOBr and $Bi_4Ti_3O_{12}$, and its band gap was measured to be 3.0 eV.

3.2. Photocatalytic CO_2 reduction performance

Photocatalytic CO_2 reduction was monitored under simulated solar light provided by a 300 W Xe lamp (Fig. S3). In order to enhance the ferroelectricity and exclude the influence of organic impurity attached to the surface of catalysts, the as-prepared $SrBi_4Ti_4O_{15}$ nanosheets (denoted as SBTO-1) were annealed at 350 °C (denoted as SBTO) and 650 °C (denoted as SBTO-2) for 2 h. Obviously, the crystalline phase remain unchanged after the annealing (Fig. S4). Commercial TiO_2 (P25) and some typical bismuth-based photocatalysts, such as $Bi_4Ti_3O_{12}$ and BiOBr nanosheets, are employed as reference samples (Fig. S5). As it is a gas-solid reaction and the catalyst reacts directly with CO_2, there are only gaseous products and no liquid products. Noticeably, $SrBi_4Ti_4O_{15}$ shows powerful CO_2 reduction ability for CH_4 and CO production, far outperforming three other catalysts (Fig. 2a and b). Particularly, CH_4 as the primary product shows a high-efficiency evolution rate of 19.8 $\mu mol\,h^{-1}\,g^{-1}$ with a high selectivity of 93% (Fig. 2c), and the apparent quantum efficiency (AQE) is as high as 1.33% at 365 nm. The CH_4 evolution rate of $SrBi_4Ti_4O_{15}$ is ~8.65 and 283 times that of $Bi_4Ti_3O_{12}$ and BiOBr, and the CH_4 evolution amount of P25 is neglectable. Cycling test repeated for 3 runs and the 8 h-continuous photocatalytic CO_2 reduction confirmed the durability and the repeatability of $SrBi_4Ti_4O_{15}$ (Fig. S6). It is important to note that the CO_2 reduction activity of $SrBi_4Ti_4O_{15}$ nanosheets exceeds those of almost all reported bismuth-based photocatalysts (modification or not) and most of reported established photocatalysts, particularly in gas-solid reaction system (Table S2). Besides, the almost unchanged XPS spectra after photoreaction reflect the high photochemical stability of $SrBi_4Ti_4O_{15}$ (Fig. S7 and 8).

In order to clarify the carbon source, a series of controlled and isotopic tracing experiments were conducted. For the $SrBi_4Ti_4O_{15}$ annealed at 350 °C (SBTO), no CH_4 or CO can be detected in the photocatalytic CO_2 reduction process with purging Ar (Fig. 2d and e). Same control test was carried out on the as-prepared $SrBi_4Ti_4O_{15}$ nanosheets without annealing (SBTO-1), trace amount of CH_4 was produced with purging Ar (Fig. 2f), indicating the presence of surface carbon. It demonstrates that calcination at 350 °C and above removes the organic impurities on the surface of catalysts. $^{13}CO_2$ isotopic tests are also performed for further confirmation. It is found from gas chromatograms that the reduction products consist of only ^{13}CO but no $^{13}CH_4$ when purging $^{13}CO_2$ into the reactor (Fig. 3a). However, CH_4 and CO were detected again when replacing $^{13}CO_2$ with $^{12}CO_2$, which are also confirmed by the isotopic mass spectra, in which ^{12}CO with *m/z* at 28 and $^{12}CH_4$ with *m/z* at 16 are observed with purging ^{12}CO, and only ^{13}CO with *m/z* at 29 is observed with purging $^{13}CO_2$ (Fig. 3b). Therefore, it is speculated that $^{13}CO_2$ restrains the formation of methane from $SrBi_4Ti_4O_{15}$, which may be caused by isotope fractionation effect. To corroborate this conjecture, the $^{13}CO_2$ photocatalytic reduction experiments are also carried out over two other typical bismuth-based photocatalysts Bi_2WO_6 and $Bi_4O_5Br_2$, which can produce both CH_4 and CO from CO_2 photoreduction. Obviously, the same phenomena with $SrBi_4Ti_4O_{15}$ were observed. Both $^{12}CH_4$ and ^{12}CO are detected when purging $^{12}CO_2$, and only ^{13}CO is produced with purging $^{13}CO_2$ (Fig. S9a and b). In view of the above phenomenon and no CO_2 reduction products detected from SBTO with purging Ar, it is confirmed that CH_4 and CO originate from CO_2 via photocatalytic reduction. For providing more solid evidence, O_2 generation from the oxidative half-reaction during the CO_2 reduction process was determined (Fig. 3c). The detected production of O_2, CH_4 and CO satisfied the transported numbers of electrons and protons in a redox reaction, which demonstrates that the CO_2 reduction and H_2O oxidation simultaneously occurred on $SrBi_4Ti_4O_{15}$ [23], and CH_4 is actually the main product for the reduction reaction.

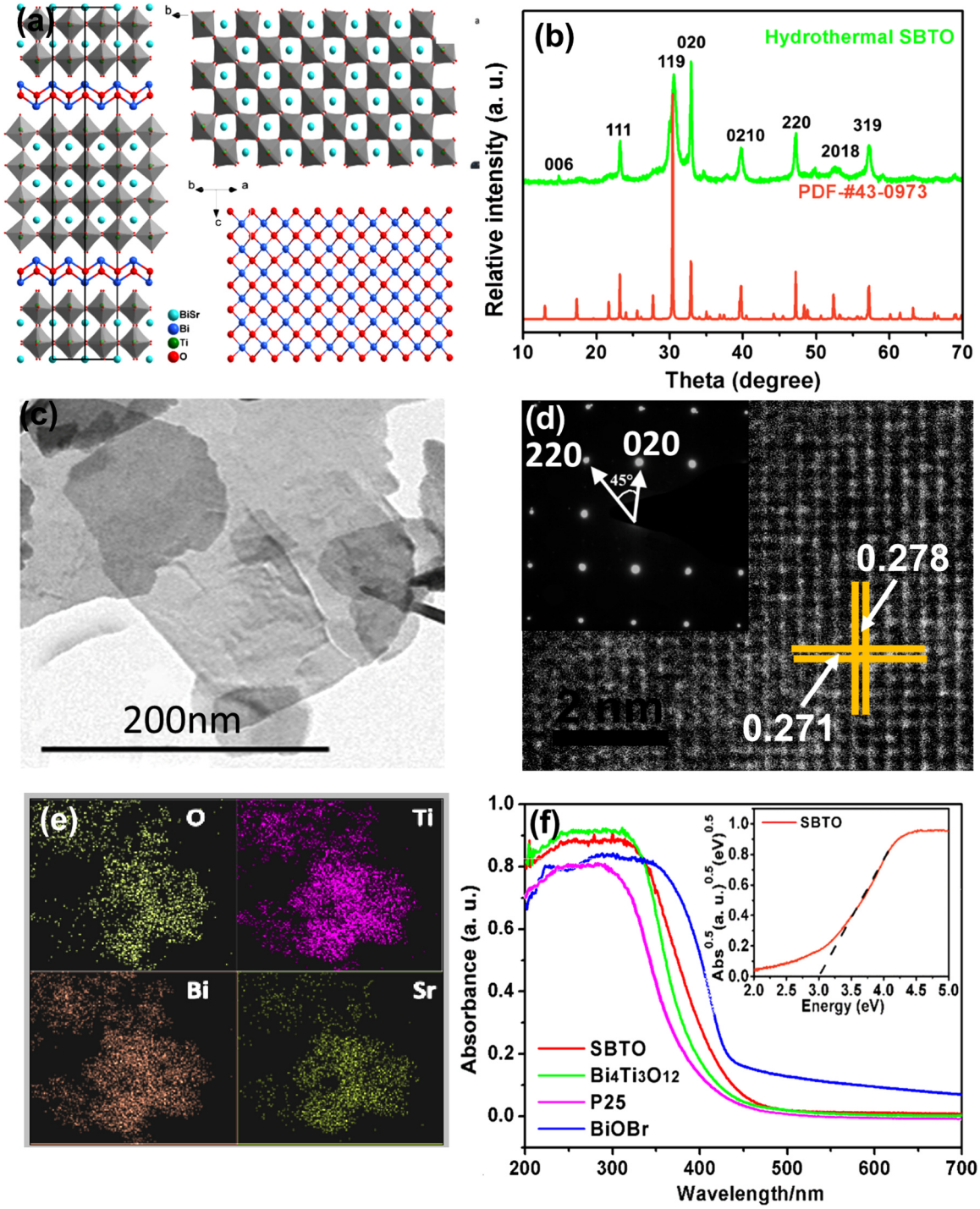

Fig. 1. (a) Crystal structure, (b) XRD pattern, (c) TEM image, (d) HRTEM image and SAED pattern (inset) and (e) EDX elemental mappings of as-synthesized $SrBi_4Ti_4O_{15}$ nanosheets. (f) UV–vis absorption of $SrBi_4Ti_4O_{15}$ (inset shows the band gap) nanosheets, $Bi_4Ti_3O_{12}$, P25 and BiOBr.

In situ diffuse reflectance infrared fourier transform spectroscopy (DRIFTS) was conducted to survey CO_2 conversion mechanism and the interfacial changes (Fig. 3d). Under CO_2 adsorption process (0–20 min), various peaks of carbonate species can be observed on the spectra of SBTO, suggesting its adsorption ability toward CO_2 molecules [24]. The C-H stretching peaks of CH_4 at 1339 cm^{-1} and CO at 2017 cm^{-1} (attributed to bridge-bonded CO on SBTO) keep growing (Fig. S10b and c) and the double strong peaks of CO_2 at 2325 and 2309 cm^{-1} (Fig. S10a) diminish considerably during the irradiation (20–60 min), indicating the conversion of CO_2 to CH_4 and CO [25]. Adsorption bands at 1410–1560 cm^{-1} and 1610–1870 cm^{-1} are assigned to the bending vibration of C–H, the stretching vibration of C=O and the asymmetric stretching of O–C=O, which belong to aldehydes, carboxylic acids, and methoxy. In view of the almost unchanged intensity of these peaks and the gas-solid reaction system, they are intermediate products [26]. Possible electron/proton transport process and the formation process of products was speculated based on the amount of final products and the qualitation of intermediate products. (Fig. S11)

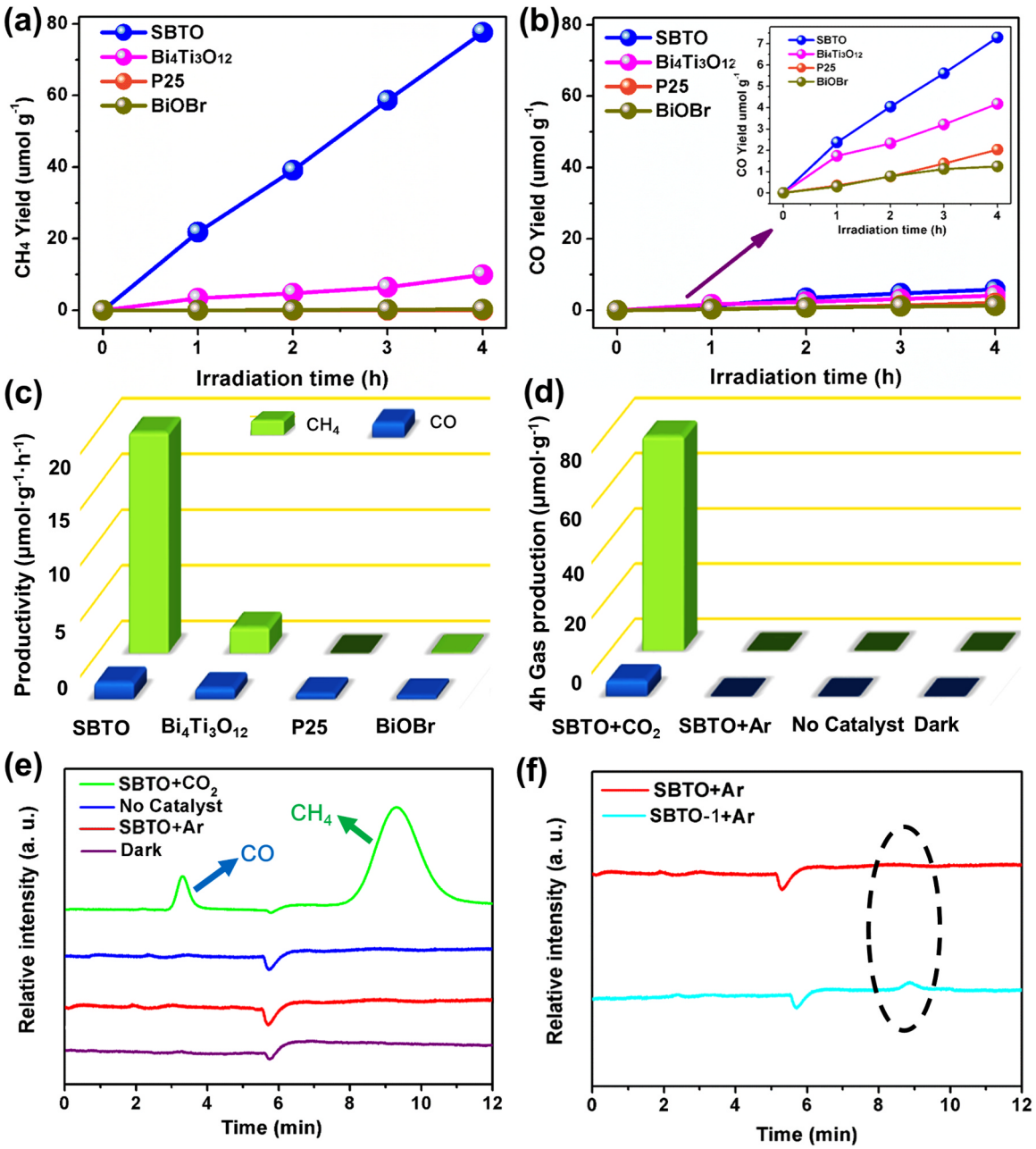

Fig. 2. (a, b) CO and CH_4 yield curves and (c) the corresponding rates over $SrBi_4Ti_4O_{15}$, $Bi_4Ti_3O_{12}$, P25 and BiOBr. (d) CO and CH_4 production and (e) the corresponding gas chromatograms under different conditions for 4 h. (f) Gas chromatograms of as-prepared $SrBi_4Ti_4O_{15}$ (SBTO-1) and $SrBi_4Ti_4O_{15}$ annealed at 350 °C (SBTO) with purging Ar.

3.3. Photocatalytic mechanism analysis based on DFT calculations and experimental results

To probe if specific surface area plays a dominant role in the CO_2 photoreduction activity of $SrBi_4Ti_4O_{15}$, gas-adsorption characteristics of the above-mentioned materials are studied (Fig. S12a and b). $SrBi_4Ti_4O_{15}$, $Bi_4Ti_3O_{12}$, P25 and BiOBr have comparable specific surface area and physical adsorption capacity, indicating that these factors are not the reason for the robust CO_2 reduction activity of $SrBi_4Ti_4O_{15}$. As photocatalytic activity is strongly influenced by the energy band levels of semiconductors [27], the band structure of $SrBi_4Ti_4O_{15}$ is investigated. The flat-band potential of $SrBi_4Ti_4O_{15}$ is determined to be −1.25 eV versus SCE. Thus, the conduction band (CB) and valence band (VB) positions are calculated to be ~-1.15 and 1.85 eV, respectively [28]. The highly negative CB level of $SrBi_4Ti_4O_{15}$ offers a strong driving force for triggering the CO_2 conversion into CH_4 or CO (Fig. 4a and b). The energy band structure of $SrBi_4Ti_4O_{15}$ is undoubtedly most suitable for CO_2 reduction in comparison with three other materials (Fig. S13).

The orbital occupancy of each atom of $SrBi_4Ti_4O_{15}$ is studied by density of states calculation (Fig. 4c and S14). The bottom of CB is mainly occupied by the Ti 3d orbitals while hybridized O 2p and Bi 6s orbitals co-participate in the formation of top of VB. Hence the photogenerated holes will primarily migrate to the $Bi_2O_2^{2+}$ layers and the electrons transfer to the Ti-O octahedral layers. As a result, effective separation of photogenerated charge carriers can be achieved in the local unit cell of $SrBi_4Ti_4O_{15}$. NCS crystal structure, in particular consisting of well-aligned distorted polyhedra, can cause a large intrinsic polarization which boosts the charge separation [29]. For ferroelectric $SrBi_4Ti_4O_{15}$, its ferroelectric polarization arises mainly from the

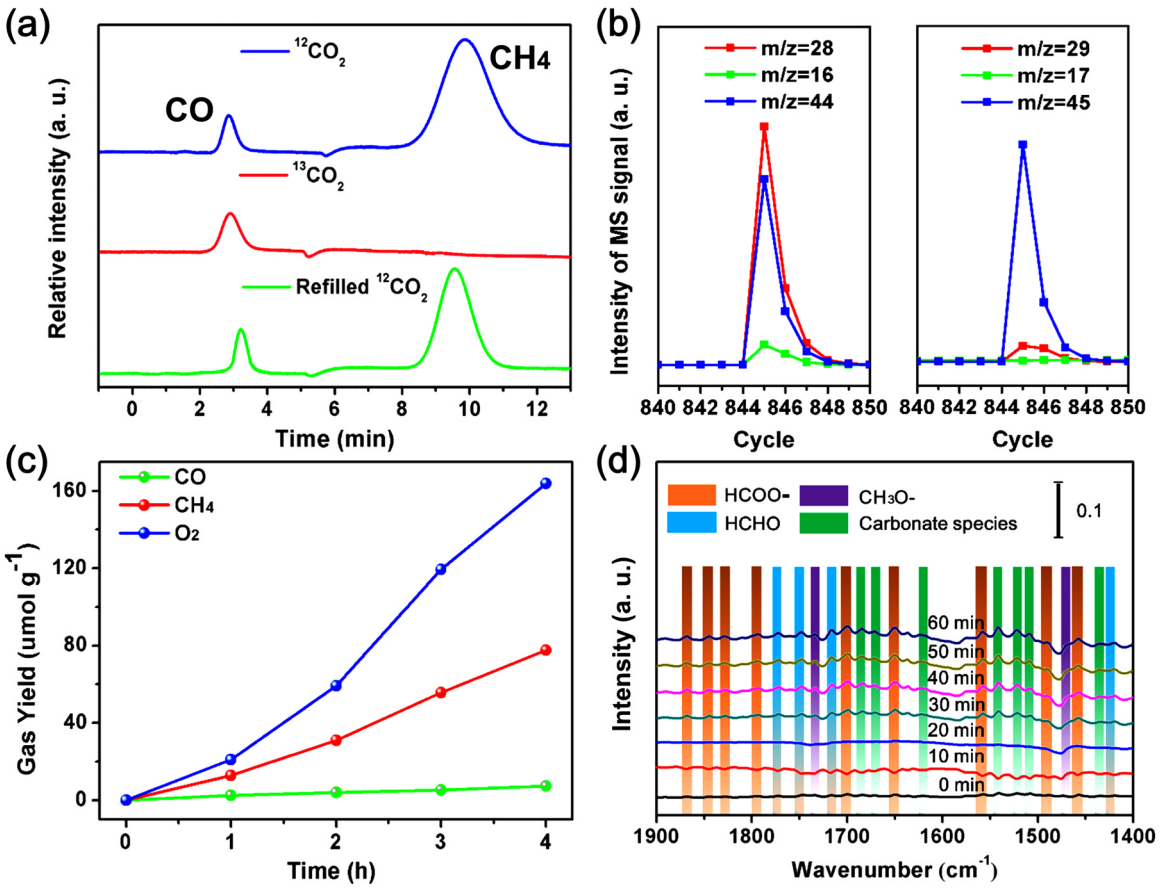

Fig. 3. (a) Gas chromatograms of SBTO with purging $^{12}CO_2$ or $^{13}CO_2$ and (b) the corresponding mass spectra siganls with $^{12}CO_2$ and $^{13}CO_2$. (c) Reductive and oxidative production curves of SBTO during CO_2 reduction and (d) *In situ* DRIFTS for CO_2 photoreduction on SBTO under Xe-lamp irradiation for different time.

distortion of TiO_6 octahedra. Along the *b* and *c* axis, the polarization of Ti-O octahedron is offset owing to the completely opposite arrangement of neighboring TiO_6 octahedra along the two directions (Fig. S15). However, the spontaneous polarization of $SrBi_4Ti_4O_{15}$ is cumulative along *α* axis due to the well-aligned distortion orientation of TiO_6 octahedra along [100] direction (Fig. 5a). Therefore, it is forecasted that a giant polarization can be generated along the [100] direction of $SrBi_4Ti_4O_{15}$.

To visualize the ferroelectricity of $SrBi_4Ti_4O_{15}$ nanosheets, piezoresponse force microscopy (PFM) is performed. The phase maps of the piezoelectric responses (Fig. 5b-d) and standard ferroelectric butterfly amplitude curve (Fig. S16a) are obtained. The two well-matched maps clearly revealed the presence of the irregularly shaped domain walls and the presence of bright and dark areas indicates the different polarization orientation. The corresponding potential difference curve of $SrBi_4Ti_4O_{15}$ (Fig. S16b) implies the different polarization and orientation in the $SrBi_4Ti_4O_{15}$ nanosheets. It indicates that the polarized electric field is formed between dark and bright regions, suggesting ferroelectric spontaneous polarization rooted in $SrBi_4Ti_4O_{15}$. The standard ferroelectric butterfly amplitude curve and phase curve of $SrBi_4Ti_4O_{15}$ are obtained by applying a ramp voltage from −5–5 V. The butterfly amplitude curve shows the apparent variation in the amplitude, which is related to the changing strain under an external field. Besides, the ferroelectric phase curve (Fig. 5e) corresponding to domain phase map exhibits an approximately 155° switching when reversing the external electric field, which also confirms the ferroelectric features of the $SrBi_4Ti_4O_{15}$ nanosheets [30]. All above characterizations provide direct evidence for the existence of ferroelectric polarization within the as-obtained $SrBi_4Ti_4O_{15}$ nanosheets.

For providing an in-depth insight into high photocatalytic CO_2 activity of $SrBi_4Ti_4O_{15}$ promoted by spontaneous polarization, effective masses of charge carriers along different directions are calculated by DFT (Table S3). A smaller effective mass favors the high mobility of charge carriers, facilitating the charge transfer process. It is important to note that the effective masses of electrons and holes along [100] direction are 0.018 and 0.014, which are far smaller than those along [010] (0.831/0.119) and [001] (1.041/0.127) directions. It demonstrates the high migration rate of electrons and hole along [100], which accords the giant polarization of $SrBi_4Ti_4O_{15}$ along *α* axis. As the polarization propels the negatively charged electrons and positively charged holes to move toward opposite directions, the recombination of photogenerated electrons and holes was significantly depressed [31–33]. Namely, the high-efficiency separation of photoinduced charge carriers of $SrBi_4Ti_4O_{15}$ is achieved by ferroelectric polarization, which greatly promotes the photocatalytic activity of $SrBi_4Ti_4O_{15}$.

Wang et al. [34] described the formation of piezo-potential in a piezoelectric materials as internal polarization generated from the nonzero dipole moment, and the piezo-potential increased with the growth of crystal length which brings an accumulation of internal polarization [35]. The separation degree of free carriers (electrons and holes) generated from an external excitation (pressure) was tremendously determined by the magnitude of piezo-potential [36], or called polarization potential. In order to verify the crucial role of ferroelectricity in promoting charge separation and photocatalysis, the ferroelectric polarization of $SrBi_4Ti_4O_{15}$ was tuned by controlling annealing temperature. Fig. 5f displays the polarization-electric field hysteresis curves of the as-prepared $SrBi_4Ti_4O_{15}$ nanosheets (SBTO-1), $SrBi_4Ti_4O_{15}$ nanosheets annealed at 350 °C (SBTO) and annealed at 650 °C (SBTO-2). Both the saturated polarization (Ps) and remnant polarization (Pr) order is SBTO > SBTO-2 > SBTO-1 at the applied

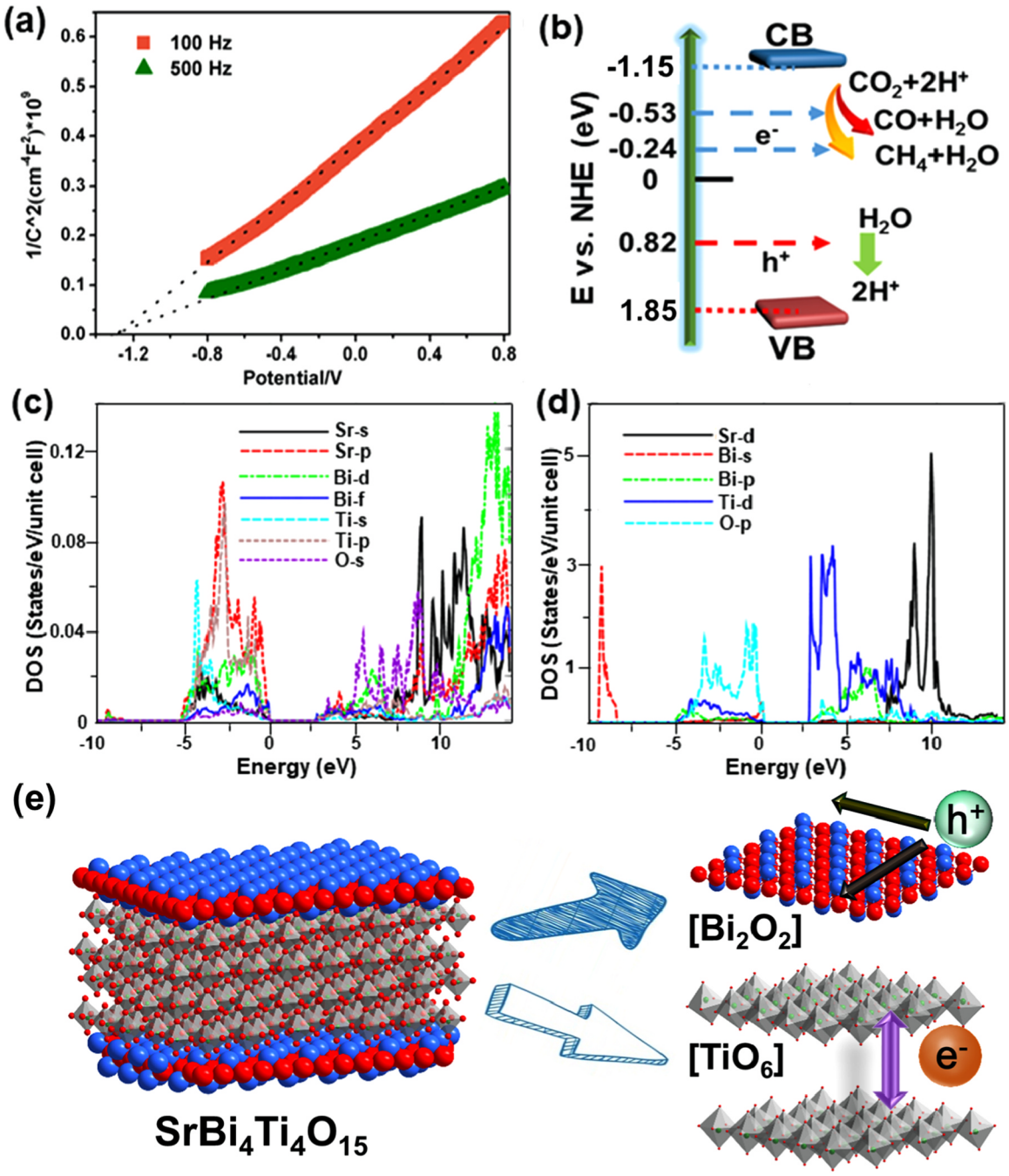

Fig. 4. (a) Motte-Schottky plots under two different frequencies and (b) diagram for the band energy levels of $SrBi_4Ti_4O_{15}$. (c, d) Density of states (DOS) of $SrBi_4Ti_4O_{15}$ and (e) schematic diagram for separation and migration of photogenerated electrons and holes along different directions in the units.

electric field of −1500 to 1500 kV/cm. The decrease of Ps and Pr with increasing the annealing temperature (from 350 to 650 °C) is explained as that: Slight amount of Bi evaporates from the sample's surface (Table S4) when the temperature rises to a certain value, which results in some structural defects and thus decreases the ferroelectric property [37]. However, the photoabsorption, band energy edge and specific surface area show no big difference among these samples annealed at different temperatures (Figs. S17–S19).

Ferroelectric polarization belongs to intrinsic polarization determined by crystal structure. Similar to piezopotential, the accumulation of ferroelectric polarization could also form the potentials throughout the materials. Once free carriers are generated from the external excitation (such as light), the electrons and holes will be separated immediately along the direction of potentials originated from intrinsic polarization (ferroelectric polarization). Thus the magnitude of ferroelectric polarization can effectively affect the rate of charge transport (Fig. 6a) and result in significantly enhanced optoelectronic performances as photopiezotronics effects does [38–40]. The photocatalytic tests reveal that the CO_2 photoreduction activity of as-prepared $SrBi_4Ti_4O_{15}$ nanosheets is enhanced by annealing, where the activity order for producing both CH_4 and CO also follows SBTO > SBTO-2 > SBTO-1, in accordance with that of Ps and Pr. Namely, SBTO with the strongest ferroelectricity displays the most efficient photocatalytic performance (Fig. 6b and c). To elucidate the relationship between ferroelectricity and photocatalysis, the ns-level time-resolved fluorescence decay and steady-state PL spectra are measured to survey their charge separation efficiency difference (Fig. 6d), and the radiative lifetimes fitted from the decay spectra [41] are summarized in

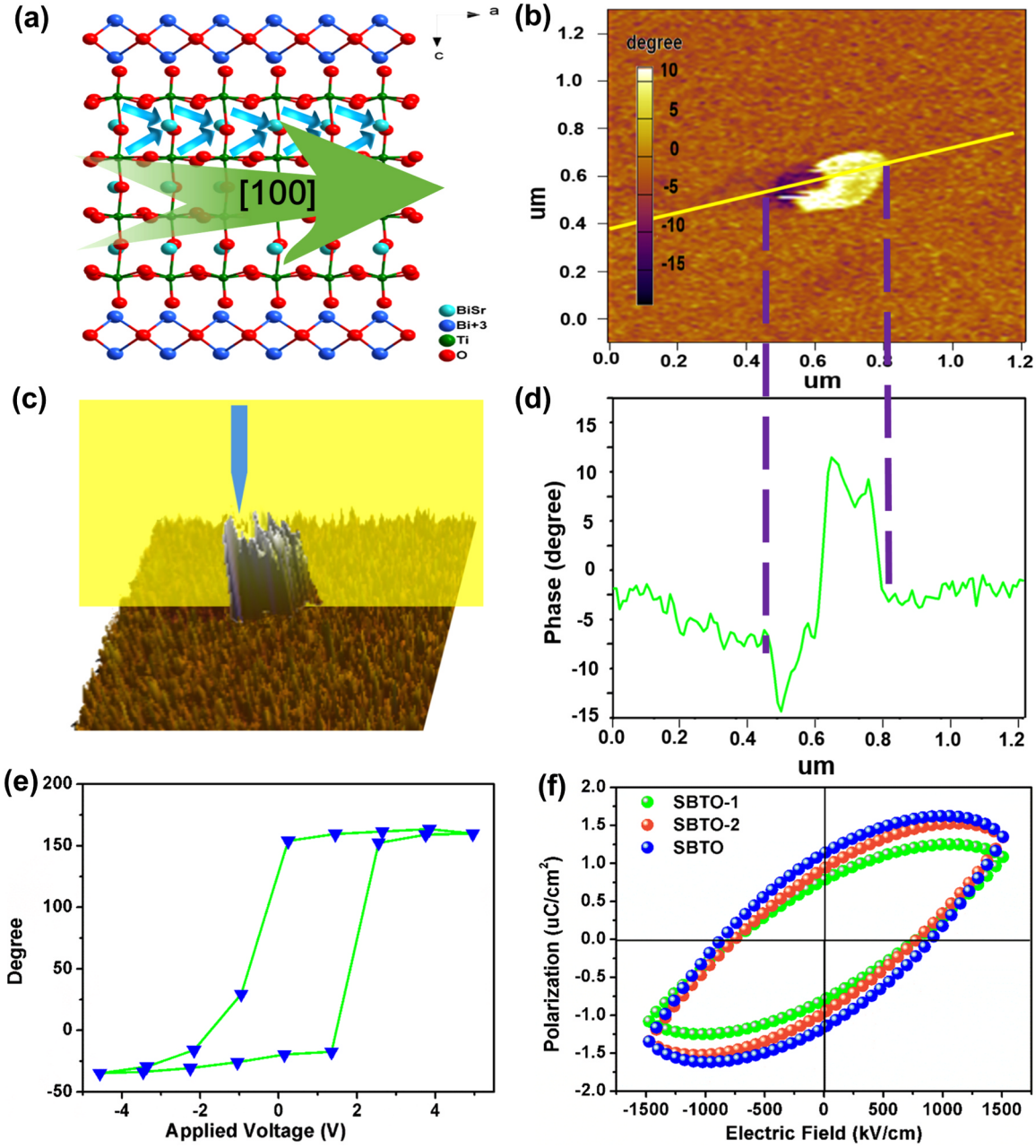

Fig. 5. (a) Polarization direction along *a* axis in the crystal structure of $SrBi_4Ti_4O_{15}$. (b) 2D, (c) 3D phase maps and (d) corresponding curve of the piezoelectric response. (e) ferroelectric phase curve SBTO obtained by PFM. (f) Electric hysteresis loop of $SrBi_4Ti_4O_{15}$ annealed at different temperatures.

Table S5. Obviously, SBTO shows both much longer short lifetime (τ1) and long lifetime (τ2) than SBTO-1 and SBTO-2, implying that the radiative lifetime of photogenerated charge carriers is prolonged with the increase of ferroelectric polarization. Steady-state PL spectra reveal that SBTO exhibits the weakest emission peak (Fig. 6e), also suggesting the lowest recombination rate of electrons and holes due to the strongest polarization [42–44]. Herein, the ferroelectric polarization serves as a strong internal potential along the [100] direction, and triggered the separation of photogenerated electrons and holes. Then, the carriers migrate along opposite directions and participate in the redox reactions on different side of surface, and any change in the magnitude of ferroelectric porlarization will cause the change in rate of carriers migration. Thus, it is established that ferroelectric polarization enhancement could serve as a promising strategy for strengthening photocatalytic activity by facilitating charge separation.

4. Conclusions

In summary, layered ferroelectric perovskite $SrBi_4Ti_4O_{15}$ nanosheets synthesized via a soft-chemical method is reported for the first time as a robust photocatalytic CO_2 reduction catalyst. $SrBi_4Ti_4O_{15}$ has strong ferroelectric spontaneous polarization along the [100] direction, which renders efficient separation and anisotropic migration of photoinduced electrons and holes. Theoretical calculations uncover that the electrons and holes separately migrate to TiO_6 octahedra and $Bi_2O_2^{2+}$ layers, and the charge carriers possess the smallest effective mass along *a* axis, highly favoring the mobility of charges along this direction. Profited from the above-mentioned advantages, $SrBi_4Ti_4O_{15}$ shows an unprecedented photocatalytic CO_2 reduction activity, with a superior CH_4 production rate of 19.8 μmol h^{-1} g^{-1} and a high apparent quantum efficiency (1.33% at 365 nm). This work shows the potential of

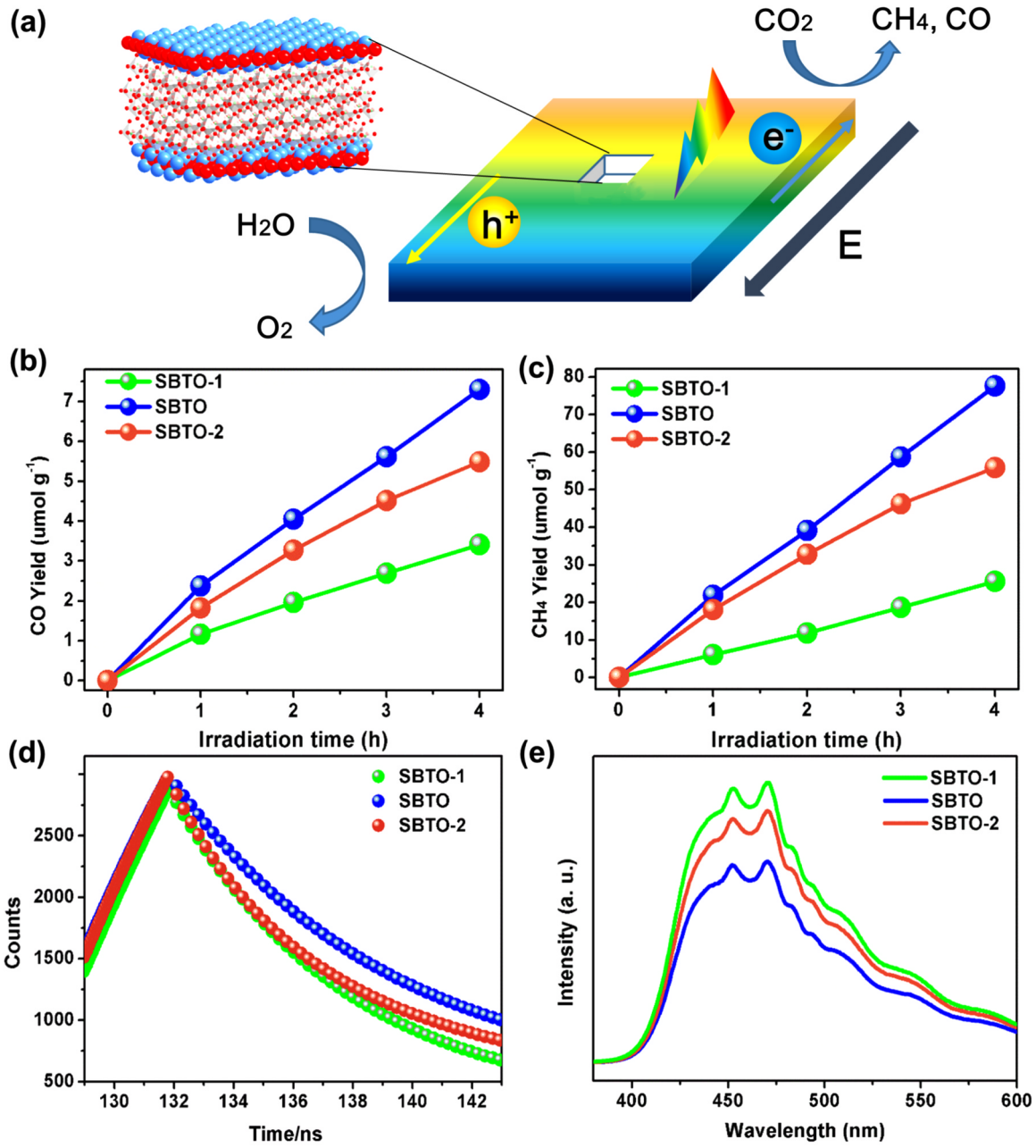

Fig. 6. (a) Schematic diagram of polarization-field enhanced separation of photogenerated charge carriers. (b) CH_4 and (c) CO yield curves, (d) ns-level time-resolved fluorescence spectra and (e) stady-state PL spectra of SBTO, SBTO-1 and SBTO-2.

ferroelectric semiconductors as a promising system to trigger bulk charge separation and migration for photo(electro)-catalysis.

Acknowledgements

This work was supported by the National Natural Science Foundation of China (Nos. 51672258, 51572246, 51602216), the Fundamental Research Funds for the Central Universities (2652015296), Australian Research Council (ARC) through Discovery Early Career Researcher Award (DE150101306) and Linkage Project (LP160100927).

Appendix A. Supporting information

Supplementary data associated with this article can be found in the online version at doi:10.1016/j.nanoen.2018.12.016.

References

[1] M.D. Kärkäs, B.S. Matsuura, C.R.J. Stephenson, Enchained by visible light–mediated photoredox catalysis, Science 349 (2015) 1285–1286.
[2] M. Liu, Y.J. Pang, B. Zhang, P. De Luna, O. Voznyy, J.X. Xu, X.L. Zheng, C.T. Dinh, F.J. Fan, C.H. Cao, F.P.G. de Arquer, T.S. Safaei, A. Mepham, A. Klinkova, E. Kumacheva, T. Filleter, D. Sinton, S.O. Kelley, E.H. Sargent, Enhanced electrocatalytic CO_2 reduction via field-induced reagent concentration, Nature 537 (2016) 382–386.
[3] H. Rao, L.C.S. Schmidt, J. Bonin, R. Marc, Visible-light-driven methane formation from CO_2 with a molecular iron catalyst, Nature 548 (2017) 74.
[4] C.W. Kim, S.J. Yeob, H.M. Cheng, Y.S. Kang, A selectively exposed crystal facet-engineered TiO_2 thin film photoanode for the higher performance of the photo-electrochemical water splitting reaction, Energy Environ. Sci. 8 (2015) 3646–3653.
[5] J.Z. Zhang, Interfacial charge carrier dynamics of colloidal semiconductor nanoparticles, J. Phys. Chem. B 104 (2000) 7239.
[6] J. Li, L.J. Cai, J. Shang, Y. Yu, L.Z. Zhang, Giant enhancement of internal electric field boosting bulk charge separation for photocatalysis, Adv. Mater. 28 (2016) 4059–4064.
[7] J. Li, G.M. Zhan, Y. Yu, L. Zhang, Superior visible light hydrogen evolution of Janus

bilayer junctions via atomic-level charge flow steering, Nat. Commun. 7 (2016) 11480.
[8] A.L. Linsebigler, G. Lu, T.Y. John, Photocatalysis on TiO_2 surfaces: principles, mechanisms, and selected results, Chem. Rev. 95 (1995) 735–758.
[9] P.V. Kamat, Manipulation of charge transfer across semiconductor interface. A criterion that cannot be ignored in photocatalyst design, J. Phys. Chem. Lett. 3 (2012) 663.
[10] W.G. Yang, Y.H. Yu, M.B. Starr, X. Yin, Z.D. Li, A. Kvit, S.F. Wang, P. Zhao, X.D. Wang, Ferroelectric polarization-enhanced photoelectrochemical water splitting in TiO_2–$BaTiO_3$ core–shell nanowire photoanodes, Nano Lett. 15 (2015) 7574–7580.
[11] J.L. Xie, C.X. Guo, P.P. Yang, X.D. Wang, D.Y. Liu, C.M. Li, Bi-functional ferroelectric $BiFeO_3$ passivated $BiVO_4$ photoanode for efficient and stable solar water oxidation, Nano Energy 31 (2017) 28–36.
[12] H.D. Li, Y.H. Sang, S.J. Chang, X. Huang, Y. Zhang, R.S. Yang, H.D. Jiang, H. Liu, Z.L. Wang, Enhanced ferroelectric-nanocrystal-based hybrid photocatalysis by ultrasonic-wave-generated piezophototronic effect, Nano Lett. 15 (2015) 2372–2379.
[13] H.W. Huang, S.C. Tu, C. Zeng, T.R. Zhang, A.H. Reshak, Y.H. Zhang, Macroscopic polarization enhancement promoting photo-and piezoelectric-induced charge separation and molecular oxygen activation, Angew. Chem. Int. Ed. 56 (2017) 11860–11864.
[14] H.W. Huang, Y. He, X.W. Li, M. Li, C. Zeng, F. Dong, X. Du, T.R. Zhang, Y.H. Zhang, $Bi_2O_2(OH)(NO_3)$ as a desirable $[Bi_2O_2]^{2+}$ layered photocatalyst: strong intrinsic polarity, rational band structure and {001} active facets co-beneficial for robust photooxidation capability, J. Mater. Chem. A 3 (2015) 24547–24556.
[15] H.J. Yu, H.W. Huang, K. Xu, W.C. Hao, Y.X. Guo, S.B. Wang, X.L. Shen, S.F. Pan, Y.H. Zhang, Liquid-phase exfoliation into monolayered BiOBr nanosheets for photocatalytic oxidation and reduction, Acs. Sustain. Chem. Eng. 5 (2017) 10499–10508.
[16] S.C. Tu, H.W. Huang, T.R. Zhang, Y.H. Zhang, Controllable synthesis of multi-responsive ferroelectric layered perovskite-like $Bi_4Ti_3O_{12}$: photocatalysis and piezoelectric-catalysis and mechanism insight, Appl. Catal. B-Environ. 219 (2017) 550–562.
[17] M.D. Keijser, G.J.M. Dormans, P.J.V. Veldhoven, D.M.D. Leeuw, Effects of crystallite size in $PbTiO_3$ thin films, Appl. Phys. Lett. 59 (1991) 3556.
[18] X.L. Zhong, J.B. Wang, X.J. Zheng, Y.C. Zhou, G.W. Yang, Structure evolution and ferroelectric and dielectric properties of $Bi_{3.5}Nd_{0.5}Ti_3O_{12}$ thin films under a moderate temperature annealing, Appl. Phys. Lett. 85 (2004) 5661–5663.
[19] Y. Bai, L.Q. Ye, T. Chen, P.Q. Wang, L. Wang, X. Shi, P.K. Wong, Synthesis of hierarchical bismuth-rich $Bi_4O_5Br_xI_{2-x}$ solid solutions for enhanced photocatalytic activities of CO_2 conversion and Cr (VI) reduction under visible light, Appl. Catal. B-Environ. 203 (2017) 633–640.
[20] S.D. Nguyen, J. Yeon, S.H. Kim, P.S. Halasyamani, BiO(IO3): a new polar iodate that exhibits an aurivillius-type $(Bi_2O_2)^{2+}$ layer and a large SHG response, J. Am. Chem. Soc. 133 (2011) 12422–12425.
[21] Y.X. Pan, Y. You, S. Xin, Y.T. Li, G.T. Fu, Z.M. Cui, Y.L. Men, F.F. Cao, S.H. Yu, J.B. Goodenough, Photocatalytic CO_2 reduction by carbon-coated indium-oxide nanobelts, J. Am. Chem. Soc. 139 (2017) 4123–4129.
[22] J.Y. Zheng, A.U. Pawar, C.W. Kim, Y.J. Kim, Y.S. Kang, Highly enhancing photoelectrochemical performance of facilely-fabricated Bi-induced (002)-oriented WO_3 film with intermittent short-time negative polarization, Appl. Catal. B-Environ. 233 (2018) 88–98.
[23] A.U. Pawar, C.W. Kim, M.J. Kang, Y.S. Kang, Crystal facet engineering of ZnO photoanode for the higher water splitting efficiency with proton transferable nafion film, Nano Energy 20 (2016) 156–167.
[24] J. Low, L. Zhang, T. Tong, B. Shen, J. Yu, TiO_2/MXene Ti_3C_2 composite with excellent photocatalytic CO_2 reduction activity, J. Catal. 361 (2018) 255–266.
[25] S. Zhu, B. Jiang, W.B. Cai, M. Shao, Direct observation on reaction intermediates and the role of bicarbonate anions in CO_2 electrochemical reduction reaction on Cu surfaces, J. Am. Chem. Soc. 139 (2017) 15664–15667.
[26] T. Wang, X. Meng, P. Li, S. Ouyang, K. Chang, G. Liu, Z. Mei, J. Ye, Photoreduction of CO_2 over the well-crystallized ordered mesoporous TiO_2 with the confined space effect, Nano Energy 9 (2014) 50–60.
[27] P. Li, Y. Zhou, Z.Y. Zhao, Q.F. Xu, X.Y. Wang, M. Xiao, Z.G. Zou, Hexahedron prism-anchored octahedronal CeO_2: crystal facet-based homojunction promoting efficient solar fuel synthesis, J. Am. Chem. Soc. 137 (2015) 9547–9550.
[28] Y.J. Chen, R.K. Huang, D.Q. Chen, Y.S. Wang, W.J. Liu, X.N. Li, Z.H. Li, Exploring the different photocatalytic performance for dye degradations over hexagonal $ZnIn_2S_4$ microspheres and cubic $ZnIn_2S_4$ nanoparticles, Acs Appl. Mater. Inter. 4 (2012) 2273–2279.
[29] X.Y. Fan, L. Zang, M. Zhang, H.S. Qiu, Z. Wang, J. Yin, H.Z. Jia, S.L. Pan, C.Y. Wang, A bulk boron-based photocatalyst for efficient dechlorination: $K_3B_6O_{10}Br$, Chem. Mater. 26 (2014) 3169–3174.
[30] L.L. Zhao, Y. Zhang, F.L. Wang, S.C. Hu, X.N. Wang, B.J. Ma, H. Liu, Z.L. Wang, Y.H. Sang, $BaTiO_3$ nanocrystal-mediated micro pseudo-electrochemical cells with ultrasound-driven piezotronic enhancement for polymerization, Nano Energy 39 (2017) 461–469.
[31] H.J. Zhang, L. Liu, Z. Zhou, First-principles studies on facet-dependent photocatalytic properties of bismuth oxyhalides (BiOXs), Rsc Adv. 2 (2012) 9224–9229.
[32] M. Dong, J.F. Zhang, J.G. Yu, Effect of effective mass and spontaneous polarization on photocatalytic activity of wurtzite and zinc-blende ZnS, APL Mater. 3 (2015) 104404.
[33] J. Yang, P.F. Jiang, M.F. Yue, D.F. Yang, R.H. Cong, W.L. Gao, T. Yang, $Bi_2Ga_4O_9$: an undoped single-phase photocatalyst for overall water splitting under visible light, J. Catal. 345 (2017) 236–244.
[34] Z.L. Wang, J. Song, Piezoelectric nanogenerators based on zinc oxide nanowire arrays, Science 312 (2006) 242–246.
[35] K.S. Hong, H. Xu, H. Konishi, X. Li, Direct water splitting through vibrating piezoelectric microfibers in water, J. Phys. Chem. Lett. 1 (2010) 997–1002.
[36] M.B. Starr, J. Shi, X. Wang, Piezopotential-Driven redox reactions at the surface of piezoelectric materials, Angew. Chem. Int. Ed. 51 (2012) 5962–5966.
[37] H. Watanabe, T. Mihara, H. Yoshimori, C.A.P. Dearaujo, Preparation of ferroelectric thin films of bismuth layer structured compounds, Jpn. J. Appl. Phys. 34 (1995) 5240–5244.
[38] J. Yang, J. Chen, Y. Liu, W. Yang, Y. Su, Z.L. Wang, Triboelectrification-based organic film nanogenerator for acoustic energy harvesting and self-powered active acoustic sensing, ACS Nano 8 (2014) 2649–2657.
[39] Y. Liu, S. Niu, Q. Yang, B.D.B. Klein, Y.S. Zhou, Z.L. Wang, Theoretical Study of Piezo-phototronic Nano-LEDs, Adv. Mater. 26 (2014) 7209–7216.
[40] W. Wu, C. Pan, Y. Zhang, X. Wen, Z.L. Wang, Piezotronics and piezo-phototronics–From single nanodevices to array of devices and then to integrated functional system, Nano Today 8 (2013) 619–642.
[41] C.W. Kim, Y.S. Son, M.J. Kang, D.Y. Kim, Y.S. Kang, (040)-Crystal facet engineering of $BiVO_4$ plate photoanodes for solar fuel production, Adv. Energy Mater. 6 (2016) 1501754.
[42] R. Zhang, Y. Dai, Z.Z. Lou, Z.J. Li, Z.Y. Wang, Y.M. Yang, X.Y. Qin, X.Y. Zhang, B.B. Huang, Layered photocatalyst $Bi_2O_2[BO_2(OH)]$ nanosheets with internal polar field enhanced photocatalytic activity, CrystEngComm 16 (2014) 4931–4934.
[43] L. Wang, S. Liu, Z. Wang, Y. Zhou, Y. Qin, Z.L. Wang, Piezotronic effect enhanced photocatalysis in strained anisotropic ZnO/TiO2 nanoplatelets via thermal stress, ACS Nano 10 (2016) 2636–2643.
[44] G. Liu, L. Ma, L.C. Yin, G. Wan, H. Zhu, C. Zhen, Y. Yang, Y. Liang, J. Tan, H.M. Cheng, Selective chemical epitaxial growth of TiO_2 islands on ferroelectric $PbTiO_3$ crystals to boost photocatalytic activity, Joule 2 (2018) 1095–1107.

Shuchen Tu is currently a Ph.D. candidate in the School of Materials Science and Engineering, China University of Geosciences (Beijing). He obtained his master degree in Materials Science and Engineering, China University of Geosciences (Beijing) in 2016. His research interests focus on the design and synthesis of layered ferroelectric materials for piezo/photo-catalysis.

Yihe Zhang is a Professor at School of Materials Science and Technology, China University of Geosciences (Beijing) and leads the Beijing Key Laboratory of Materials Utilization of Nonmetallic Minerals and Solid Wastes, School of Materials Science and Technology, China University of Geosciences (Beijing). Zhang received his Ph.D. from Technical Institute of Physics and Chemistry, Chinese Academy of Sciences in 2005, and undertook a Visiting Scholar, Postdoctoral Fellow and Research Fellow in City University of Hong Kong and The Hong Kong Polytechnic University from 2003 to 2009. His current research focuses on nanomaterials, composites and their applications for environment and energy.

Ali H Reshak is a Professor at Nanotechnology and Catalysis Research Center (NANOCAT), University of Malaya. His search focuses on novel materials with promising structural, thermoelectric, optical, and other properties. The theoretical methods of studying the relationship between structure and the above mentioned properties.

Dr. Sushil Auluck obtained his doctoral degree at the University of Chicago, USA, working under the supervision of Prof. R W Stark. He joined the University of Roorkee (now IIT Roorkee) in 1978. He joined the Physics Department as Visiting Faculty on November 2007. His area of research is Condensed Matter Theory. Now he works in Indian Institute of Technology and National Physical Laboratory as Consultant. His research work is in the broad area of electronic structure calculations. His interests are fermi surfaces, band structure, magnetism, optical properties and magneto-optical properties of crystalline solids.

Liqun Ye works at Nanyang Normal University as an Assistant Professor. He got Ph.D. degree in chemistry from Wuhan University (2008–2013) and worked in professor PK Wong's group as a Research Assistant in The Chinese University of Hong Kong (2015–2016). His current research interest is to develop efficient photocatalytic approaches to solar energy conversion and utilization.

Xiaopeng Han received his B.Sc. degree in Tianjin University (2010) and Ph.D. in Nankai University (2015). He then joined the School of Materials Science and Engineering at Tianjin University. His current research interests focus on the controlled synthesis and interfacial engineering of metal-based hybrid micro-nanostructures for electrocatalysis and metal-air battery/water-splitting technologies.

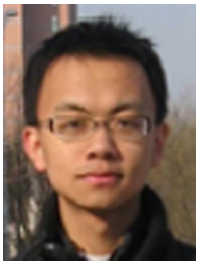

Tianyi Ma received his Ph.D. in 2013 from Nankai University, China. Then he worked as a postdoctoral research fellow from 2013 to 2014 in University of Adelaide, Australia. He was awarded Australian Research Council (ARC) Discovery Early Career Researcher Award (DECRA) in 2015, and continued independent research on the rational design of nanostructured materials with a large variety of components from carbons, metals, metal oxides, organic polymers, to metal–organic frameworks. He especially aims at the energy and environment related applications of these functional materials including catalysis, adsorption and separation, and energy conversion and storage.

Hongwei Huang received his Ph.D. in 2012 from Technical Institute of Physics and Chemistry, Chinese Academy of Sciences. Currently, he is a Professor at Beijing Key Laboratory of Materials Utilization of Nonmetallic Minerals and Solid Wastes, School of Materials Science and Technology, China University of Geosciences (Beijing). His current research mainly focuses on the design and synthesis of layered nanomaterials and functional crystals and their applications for environment and energy.